

Title	Performance improvement of MEMS Electromagnetic Vibration Energy Harvester using optimized patterns of micromagnet array
Authors	Paul, Kankana;Mallick, Dhiman;Roy, Saibal
Publication date	2021-06-10
Original Citation	Paul, K., Mallick, D. and Roy, S. (2021) 'Performance improvement of MEMS Electromagnetic Vibration Energy Harvester using optimized patterns of micromagnet array', IEEE Magnetics Letters. doi: 10.1109/LMAG.2021.3088403
Type of publication	Article (peer-reviewed)
Link to publisher's version	https://ieeexplore.ieee.org/document/9451592 - 10.1109/LMAG.2021.3088403
Rights	© 2021, IEEE. Personal use of this material is permitted. Permission from IEEE must be obtained for all other uses, in any current or future media, including reprinting/republishing this material for advertising or promotional purposes, creating new collective works, for resale or redistribution to servers or lists, or reuse of any copyrighted component of this work in other works.
Download date	2025-05-21 04:38:33
Item downloaded from	https://hdl.handle.net/10468/11470



UCC

University College Cork, Ireland
Coláiste na hOllscoile Corcaigh

Electromagnetics

Performance improvement of MEMS Electromagnetic Vibration Energy Harvester using optimized patterns of micromagnet array

Kankana Paul¹, Dhiman Mallick², and Saibal Roy^{1,3}

¹ Micro-Nano-Systems-Centre, Tyndall National Institute, Cork, T12R5CP, Ireland

² Department of Electrical Engineering, IIT Delhi, New Delhi, 110016, India

³ Department of Physics, University College Cork, Cork, T12YN60, Ireland

Abstract—Scavenging mechanical energy from ubiquitous vibrations through miniaturized electromagnetic (EM) transducers has become a potential solution to the powering issue of wireless sensor networks for the Internet of Things (IoT). This work proposes the design and performance analysis of fully integrated MEMS EM Vibration Energy Harvesters (EM-VEH). Through analytical formulation and thorough finite element analysis, we present a systematic design study to optimize the magnet-coil interaction in a precise location within a small footprint. The compact device topology yielded an EM coupling as high as 62.9mWb/m with the optimized stripe-shaped micro-magnets and rectangular micro-coils. The nonlinear spring topology demonstrated six times improvement in the half-power bandwidth compared with its linear counterpart, at the cost of reduced power density. The proposed designs can be implemented using standard MEMS fabrication methods leveraging the CMOS compatible integration at the system level for potential applications in the IoT.

Index Terms— Electromagnetics, Demagnetizing field, Patterned Magnet, Electromagnetic Coupling, Electromagnetic Vibration Energy Harvester, In-plane vibration.

I. INTRODUCTION

The widespread utilization of low power wireless sensor networks (WSNs) in this era of Internet of Things (IoT) demands a sustainable power source to replace batteries. Scavenging mechanical energy from ubiquitous ambient vibration has drawn significant research focus [Kuang 2017] as a potential solution to such powering issue. In terms of reliability and longevity, the Electromagnetic Vibration Energy Harvester (EM-VEH) outpaces the piezoelectric and electrostatic transducers, which suffers from ageing owing to the depolarization [Liao 2015] or discharge issue [Miwatani 2016]. Although the macroscale EM-VEH [Paul 2021] outpaces the contemporary transducers, the major roadblock in the implementation of a high-efficiency MEMS scale EM-VEH is the lack of high energy density miniaturized permanent hard magnets compatible with the established Integrated Circuit (IC) fabrication technology [Roy 2019]. The detrimental effect of the shape-dependent demagnetizing field [Coe 2011] reduces the stray magnetic field lines emerging from the conventionally used thin film of magnets [Han 2014, Mallick 2019], which in turn degrades the overall performance of the EM-VEH. Most of the developed MEMS EM-VEH are resonant type [Li 2020, Kulkarni 2006], which are not suitable for extracting substantial mechanical energy from the real-world non-stationarity and broadband vibrations. Inclusion of nonlinearity through geometric manipulation of the associated spring structures [Mallick 2014, Liu 2014, Roy 2021] has become a well-accepted approach to implement wideband energy harvesters. Subjected to large out-of-plane displacements, such springs demonstrate nonlinear restoring force that aids in widening the bandwidth of operation of the device. On the other hand, in-plane moving structures not only facilitates stronger EM interaction between the coil and the magnet edges but also reduces the overall profile of the device as compared with its out-of-plane counterpart [Han 2014], however, the development of in-plane moving stretching based nonlinear device is still relatively unexplored.

This letter provides an insight into the tunability of the magnetic field lines emerging from suitably micropatterned magnets and shows a systematic approach through analytical formulation and detailed finite element analysis for the optimization of the corresponding magnetic flux density. We provide a firm road map to increase the EM coupling of the coil magnet assembly vis-à-vis output power density from narrowband (linear) as well as wideband (nonlinear) MEMS scale EM-VEHs by employing square and rectangular coil geometry. Novel in-plane moving linear and nonlinear MEMS spring architectures is presented. Four novel topologies have been proposed to integrate the coil and magnet in a compact MEMS transducer that can be implemented using batch-fabrication methodologies. The overall performance of these device is compared in terms of bandwidth and obtained power density, highlighting the trade-off between the two.

II. DESIGN AND FINITE ELEMENT ANALYSIS

A. FEA and Optimization of magnetic flux density

The EM-VEH works based on the Faraday's principle of induction in which the relative motion between the magnet and the coil induces voltage (V) into the later, and this voltage is proportional to the rate of change in magnetic flux passing through the coil-

$$V = -N \frac{d\phi}{dt} = -N \cdot \frac{d\phi}{dx} \cdot \frac{dx}{dt} = -N \cdot v \cdot \frac{d\phi}{dx} = -N \cdot v \cdot \frac{dB_{effective}}{dx} \cdot \sum_{i=1}^N A_i \quad (1)$$

where, N is the number of turns in the coil v is the velocity with which the coil and the magnet move with respect to each other, $\frac{dB_{effective}}{dx}$ is the gradient of the associated magnetic flux density and A_i represents the area of an individual turn of the coil. The induced voltage and hence the output power of an EM-VEH can be enhanced by intensifying the strength and the variation of the magnetic flux density i.e. by boosting the EM coupling associated with the magnet-coil assembly.

Corresponding author Saibal Roy, Tyndall National Institute, University College Cork, Address: Lee Maltings, Dyke parade, Cork, Ireland, T12 R5CP, Phone: +353 21234 6331, Email: saibal.roy@tyndall.ie

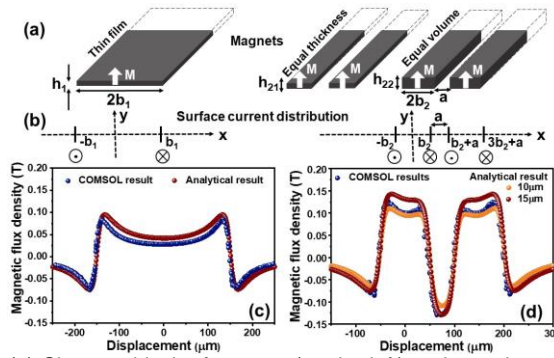


Fig.1 (a) Shows a block of magnet (on the left) and a replacement of the magnet with stripe patterns separated by a distance 'a' (on the right) having out-of-plane magnetization, (b) depicts the surface current representation of the magnets in (a), (c) and (d) shows the distribution of the vertical component of magnetic flux density on a plane that is 10 μ m away from the top surface of the magnet and stripe patterns respectively.

Conventionally, thin film of permanent magnet (as shown in Fig. 1(a)) is employed for the microscale transducers. However, the detrimental effect of the shape-dependent 'Demagnetizing field' (H_d) causes the stray magnetic fields to emanate mostly from the edge of the magnet, leaving the rest of the magnet relatively ineffective. The vertical component of magnetic flux density of an infinitely long thin film ($2b_1 = 300\mu\text{m}$, $h_1 = 10\mu\text{m}$) of a magnet can be expressed as [Furlani 2001 (207-333)],

$$B_1 = \frac{\mu_0 M_s}{2\pi} \left\{ \tan^{-1} \frac{2h_1(x+b_1)}{(x+b_1)^2 + y^2 - h_1^2} - \tan^{-1} \frac{2h_1(x-b_1)}{(x-b_1)^2 + y^2 - h_1^2} \right\} \quad (2)$$

where, μ_0 is the permeability of free space, M_s is the saturation magnetization of the material (for example, sputtered NdFeB, saturation magnetization~1T), h_1 is the height of the magnetic element, and $2b_1$ is the width of the magnet. Now if we replace this block of magnet by a couple of smaller magnetic elements ($2b_2 = 100\mu\text{m}$) having an interspacing $a = 50\mu\text{m}$, then the vertical component of magnetic flux density, considering out-of-plane magnetization, takes the form,

$$B_2 = \frac{\mu_0 M_s}{2\pi} \left\{ \tan^{-1} \frac{2h_2(x+b_2)}{(x+b_2)^2 + y^2 - h_2^2} - \tan^{-1} \frac{2h_2(x-b_2)}{(x-b_2)^2 + y^2 - h_2^2} + \tan^{-1} \frac{2h_2(x-b_2-a)}{(x-b_2-a)^2 + y^2 - h_2^2} - \tan^{-1} \frac{2h_2(x-3b_2-a)}{(x-3b_2-a)^2 + y^2 - h_2^2} \right\} \quad (3)$$

The vertical component of magnetic flux density from the thin film's edge at a distance of 10 μ m from the top of the magnet peaks to 0.09T (Fig. 1(c)), however, it reduces to 0.04T at the middle of the thin film. The increased number of magnet element edges of the stripe patterns (Fig. 1(d)) aids in intensifying the magnetic flux density peaks (0.15T), as well as the spatial variation of magnetic flux density in x-direction significantly, as compared with a continuous thin film [Zablotskii 2010, Han 2014]. Strengthening the magnetic flux density in z-direction is just as important as enhancing the gradient of magnetic flux density to improve the performance of the MEMS EM-VEHs, since the coil need to be placed very close to the magnets for it to experience any periodic magnetic field variation. While replacing the thin film with a patterned array of magnets, keeping the occupied area same, substantial magnetic volume is compromised, which accounts for the interspacing between the elements in the array. Hence to make an even comparison, the magnetic volume lost in the interspacing is compensated by altering the height of the magnets (15 μ m) in the array as shown in Fig. 1(d). This strategy could bring a significant improvement when a larger array of such magnetic elements is considered, which has been shown in the later section. Furthermore, 'Magnetic Fields (mf)' module of COMSOL Multiphysics has been

used to depict the variation of magnetic flux density for the same magnetic structures through finite element analysis. This has been shown in blue in Fig. 1(c) and (d) which agrees well with the obtained analytical results.

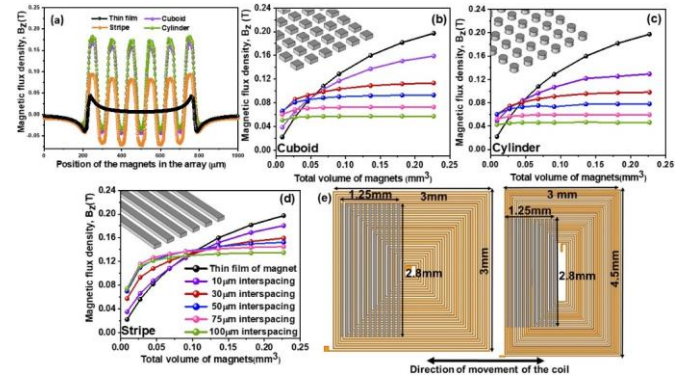


Figure 2: (a) Comparison of the z-component of magnetic flux density for different shapes of magnets having equal volume to that of a thin film of 10 μ m thickness. Plots of average magnetic flux density as a function of the total magnetic volume on a plane of observation 10 μ m away from the top of the array of magnets having (b)cuboid, (c)cylinder, (d)stripe-shaped elements are shown. (e) Shows schematic of the square (left) and rectangular copper coil (right) used with the stripe patterned magnets.

Next, we study the efficacy of different geometrical shape and the effect of interspacing of the magnetic elements in the array, in generating larger magnetic flux density in z-direction (Fig.2). Keeping in mind the fabrication complexity, in this study, we only explore the viability of simple shapes- cuboids, cylinders and stripes. The diameter of the cylinders and the width of the cubes, stripes are considered to be 50 μ m. The length of each of the stripe and arrays of patterned cuboids and cylinders is 1650 μ m. Fig. 2(a) shows the mapping of z-component of magnetic flux density on a line of observation 10 μ m away from the top of the magnets. The peak value of the periodic magnetic flux density variations for different shapes of magnets in this case increases dramatically to 0.09T, 0.17T and 0.18T for the stripe, cuboid and cylindrical shaped patterns respectively as compared with that of the thin film. This can be attributed to more magnet edges that result in substantially improved stray magnetic fields close to the line of observation in case of the cube or cylinder compared with the stripes. Although the magnitude of the stray field is greater for the cuboid and the cylinder, but when the coil interacts with the overall array, the adjacent elements of the magnet array destructively interact and deteriorate the overall magnetic flux density. Hence, to find the overall average magnetic flux lines that will interact with the coil and enhance the EM interaction, considering a surface averaged magnetic flux density is a more reliable parameter of comparison.

In the following study for each of the shape in the magnet array, the inter-element gap has been varied from 10 μ m to 100 μ m, keeping the overall area fixed to 1650 $\mu\text{m} \times 550\mu\text{m}$. The number of micromagnets along the shorter side of the array varies from 9 to 4, and the number of elements on the longer side of the 2-dimensional array changes from 28 to 12 (apart from the long stripe patterns) when the interspacing between the magnetic elements in the array is changed from 10 μ m to 100 μ m. The thickness of the thin magnetic film is varied from 10 μ m to 250 μ m. To replace the magnetic volume of this thin film with array of micromagnets, the height of each of the magnetic element in the array is altered keeping the total volume fixed, for each thickness of the thin film. The variation of the average magnetic flux density of the whole array of micromagnets as a function of the total magnetic volume is plotted

(the magnetic flux density is averaged at the observation plane, which is a distance of 10 μm). Fig.2 (b-d) depicts this variation for micromagnet arrays for different inter-element spacing (10-100 μm), with the magnetic flux density variation of the thin film of magnet shown in black as a reference. When considering low volume (equivalent thickness of thin film lying between 10 μm to 100 μm), the increased edges in the micromagnets aids in the emergence of a stronger stray magnetic field from all of the patterned magnet array having moderate interspacing (30 μm - 50 μm). But with smaller interspacing (\sim 10 μm), the magnetic flux density reduces due to the destructive magnetostatic interaction between the adjacent elements in the array. Among the patterns, the stripe shape shows superior magnetic performance which can be attributed to its long undivided sides, aiding in intensifying the magnetic flux density.

As the thin film's thickness is increased, the average magnetic flux density of the thin film outpaces that of the micromagnets- firstly, due to the absence of negative magnetostatic interaction between the neighboring elements that takes place in the micromagnets array (for relatively smaller interspacing), and secondly, owing to the reduced effect of shape-dependent demagnetizing field in relatively thicker film, the stray fields emanating from the film is stronger. Considering the MEMS-scale batch fabrication of devices and the associated packaging, we have focused on thinner magnetic films (10 μm to 100 μm thick) which could be implemented through electrodeposition [Mallick 2019], sputtering [Dempsey 2013] or pulsed laser deposition (PLD) [Nakano 2015]. To summarize, the benefits of using the patterned array of magnets can be fully exploited for a MEMS EM-VEH where thin magnetic source (up to 100 μm thick) is desired. In such case the stripe patterned magnets with moderate interspacing (\sim 50 μm) is superior to the thin films in producing substantial stray magnetic field as is evident from the analysis above.

B. Design Strategy

With the motivation of enhancing the overall performance of MEMS EM-VEHs, we have proposed four device topologies (Fig.3). Two different coil topology has been considered here- a rectangular and a square-shaped microfabricated coil having the coil resistance [Beeby 2009] (R_c) 266 Ω and 165 Ω respectively with 144 turns (as shown in Fig.2(e)). The in-plane moving silicon MEMS spring holds the microcoils on the central paddle, and additional substrate layer is assembled that carries the patterned micromagnets (as shown in Fig.3). For this analysis, we have considered an array of stripe-shaped micromagnets with 50 μm inter-element spacing, each element having 2.8mm length, 0.05mm breadth and 0.96mm height as a replacement of a 50 μm (height) thin film having lateral dimensions of 2.8mm \times 1.25mm. In Topology-1, the magnets are only on one side of the microcoil. For topology-2, oppositely polarized patterned magnets have been used to induce a large magnetic flux gradient across the coil. In topology-3, another substrate layer containing the oppositely polarized stripe magnets are bonded at the bottom of the MEMS spring. Since all of the stripe shapes magnets are assigned out-of-plane magnetization, the vertically emerging field lines form a close loop across the microcoil. Although, the polarization of the magnets on the top and bottom of the coil also aids in closing the flux lines around the coil, however, a significant share of the emerging magnetic field lines from the patterned magnets fringes out and fails to interact with the coil efficiently. Hence, in topology-4, to minimize the divergence of stray fields emerging from the magnet array, additional layers of soft magnetic material are incorporated on the side of the magnet array away from the coil. The top and bottom patterned magnet assembly in topology-4 aids to direct the magnetic field lines more towards the coil to substantially enhance the EM interaction.

Two types of MEMS spring (in-plane moving) have been designed to implement the conceived topologies using the 'structural mechanics module' of COMSOL Multiphysics. One spring is resonant type comprising a 4.5mm \times 3mm central paddle connected to the outer fixed support through a pair of 1.9mm long and 50 μm meandered arms (Fig. 4(a)). The other spring structure consists of

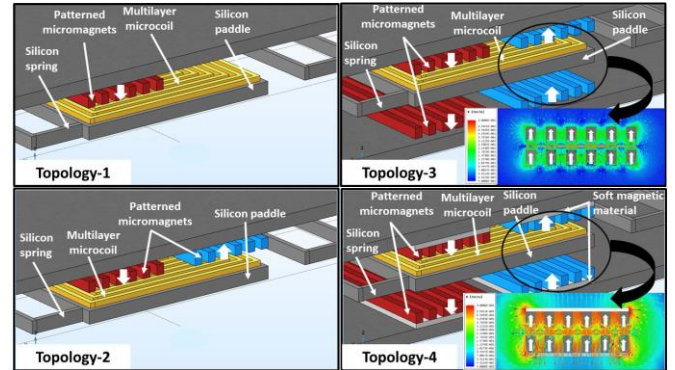


Figure 3: Proposed topologies for the MEMS EM-VEH.

thin short beams (each having 1800 μm length and 30 μm width) between the fixed support and the in-plane moving central paddle which demonstrates nonlinear restoring force (nonlinear spring stiffness coefficient 1.76×10^{11} N/m³) owing to the stretching under large amplitude deflection (Fig. 4(b)) [Paul 2019]. The fundamental modes of vibration of the linear and the nonlinear spring architectures are at 614Hz and 605Hz respectively. The total volume of the MEMS device is 0.05cm³ and 0.06cm³ for the linear and the nonlinear architecture, respectively.

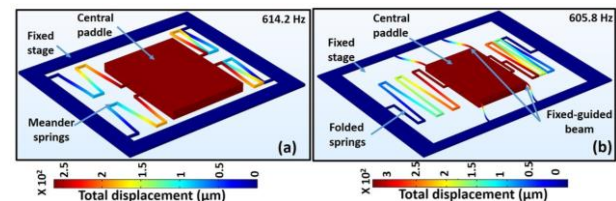


Figure 4: Fundamental modes of oscillation of the designed (a) Linear (b) Nonlinear MEMS spring structures.

To study the effect of nonlinearity on the overall performance of the VEHs, along with the nonlinear spring architecture demonstrated in Fig. 4(b) (which is referred to as (d) in Fig. 5), we designed three other MEMS springs that possess nonlinear stiffness coefficients which differs by orders of magnitude. Fig. 5(a) shows a nonlinear spring in which the nonlinear thin springs attached with the fixed stage has been modified into a folded beam form. This lower the nonlinear spring stiffness coefficient to 5.01×10^7 N/m³. In the consecutive architectures as well, the nonlinear stiffness coefficient has been changed from 2.95×10^8 N/m³ in (b) to 4.38×10^{10} N/m³ in (c) as the stretchable springs are changed from typical meandered shape to stepped thin beams.

III. RESULTS AND DISCUSSION

The electrical energy produced from scavenging the ambient mechanical energy, is extracted across the electrical damper [Lei 2015] of an EM-VEH. The power extracted across a suitable load resistance R_L over a period of oscillation can be expressed as –

$$P_L = \int_0^T \frac{\gamma^2 R_L}{(R_C + R_L)^2} \left(\frac{dx}{dt} \right)^2 dt \quad (4)$$

Where, (dx/dt) is the velocity of the harvester movement for in-plane

motion, γ is the EM coupling factor ($=N \cdot d\phi/dx$) between the coil (with resistance R_c) with N turns that experiences a gradient of magnetic flux linkage ($d\phi/dx$) and T is the time period of oscillation. So, to enhance the overall performance of MEMS EM-VEH, we investigate the effect of different coil geometries on the EM coupling. A rectangular (4.5mm X 3mm X 0.01mm) and a square (3mm X 3mm X 0.01mm) shaped micro coil (144 coil turns) has been employed. Ansoft Maxwell simulation tool has been used to investigate the EM interaction between these coils and the micromagnets through transient analysis. For this study, we have considered sputtered NdFeB material with a coercivity of 924kA/m and retentivity of 1.23T [Orlandini-Keller 2020]. The volume of a 50 μ m thin film of permanent magnet has been replaced by 13 stripe shaped micromagnets, each having dimension 2.8mm X 0.05mm X 0.96mm, to manipulate the emanating stray magnetic field. The height of each stripe has been adjusted to compensate the loss of magnetic volume in the interspacing between the magnets in the array. Table-1 summarizes the EM coupling obtained using both of the coils. Irrespective of the type of magnet arrangements chosen, the coefficient of the EM interaction is almost the same with square shaped micro coil. Only in the case of Topology-4, the stripe magnets yielded an improved EM coupling of 38.37mWb/m over that of the thin film.

Table 1. Value of the EM coupling obtained from FEM analysis with different topologies of EM-VEH

Topology	EM coupling with Square coil (mWb/m)		EM coupling with Rectangular coil (mWb/m)	
	Thin Film	Stripe pattern	Thin Film	Stripe pattern
1	4.47	4.08	7.36	8.42
2	9.08	8.79	13.61	19.45
3	15.71	14.89	26.07	24.11
4	31.66	38.37	48.05	62.9

Rectangle shaped microcoil with Topology-1 results in an EM coupling of 7.36mWb/m for a 50 μ m thin film, which increases to 8.42mWb/m with a comparable array of stripe micromagnets. The EM coupling improves with the rectangular coil as the stray magnetic fields emerging from each side of the long edges of the patterned/unpatterned magnets interacts with the parallel tracks of the coil longitudinally when the central paddle of the MEMS spring exhibits in-plane vibrations. However, due to the geometrical shape of the square coil, significant fraction of the coil tracks are in the transverse direction with respect to the micromagnets which does not promote substantial EM interaction between the coil turns and magnetic field lines resulting in lower EM coupling. On external excitation when the rectangular shaped coil on the central paddle of the MEMS spring exhibits in-plane motion, the stray magnetic fields emerging from each side of the long edges of stripe patterned magnets interacts with the parallel tracks of the coil. In Topology-2, with oppositely polarized adjacent magnet layer, the stripe magnet shows superior interaction with the coil than that with thin film, contributing an EM coupling of 19.45mWb/m. However, in the third topology that consists of four arrays of magnets, having the adjacent array oppositely polarized, the fields lines from the stripes fringes out while forming a close flux line between the magnets. To substantially reduce the divergence of the magnetic field lines and to further increase the EM coupling, in Topology-4 an additional layer of soft magnetic material is added on the base of each magnet array. We have used Ni₄₅Fe₅₅ electrodeposited (thickness 20 μ m) alloy as the soft magnetic material with the saturation magnetization of 1.2X10⁶ A/m [Jamieson 2013]. This layer aids to concentrate the magnetic field lines emanating from the oppositely polarized patterned magnets towards the coil, as shown in the insets of Fig.3.

A substantial improvement in the EM interaction could be observed using this soft magnetic base in topology-4 with the stripe magnet array and rectangular coil which enhances the EM coupling factor from 24.11mWb/m in topology-3 to 62.9mWb/m in topology-4. This proves the efficacy of integrating qualitatively optimized patterned magnets instead of continuous thin films to overcome the detrimental effect of the demagnetizing field.

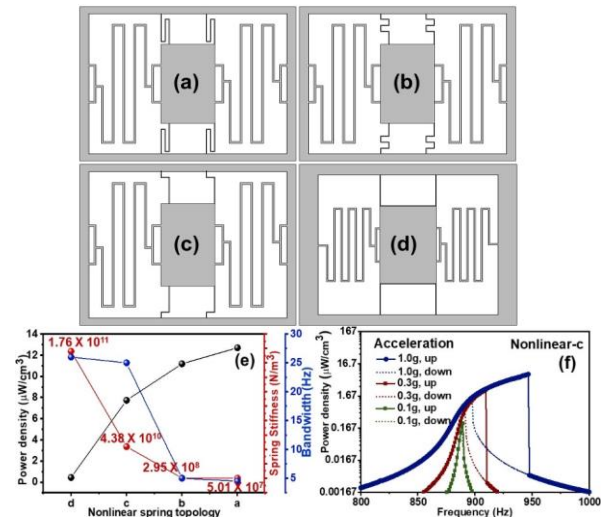


Figure 5: (a,b,c,d) Shows four nonlinear spring architecture with varying nonlinear spring stiffness coefficient. (e) Shows variation of power density and half-power bandwidth with respect to the nonlinear spring stiffness. (f) Shows the variation of load power density of spring-c with frequency.

Now to evaluate the electro-dynamical performance of different nonlinear device topologies, we have considered here all the four nonlinear spring structures that are shown in Fig. 5 (a,b,c,d) to be assembled in Topology-4, each of them offering degree of nonlinearity differing by order of magnitude. From Fig.5(e) we can observe that, as the coefficient increases, the spring becomes harder to move due to the induced spring hardening nonlinearity. Although this enhances the half-power bandwidth from 5Hz (which is close to that of the linear system offering the bandwidth of 4Hz) in spring-a to 26Hz in spring-d, but it also restricts the motion of the spring which in turn affects the interaction between coil and magnet, hence the induced voltage. The power density, in this case, falls from 12.7 μ W/cm³ for spring-a to 0.45 μ W/cm³ for spring-d. Hence, to compare the performance of the conceived linear and the nonlinear topologies, we have selected the nonlinear spring-c (having a moderately high power density of 7.73 μ W/cm³ along with high half-power bandwidth of 25Hz) along with the linear spring (Fig.4(a)) architecture. Fig. 5(f) shows the dynamic characteristics of the nonlinear MEMS EM-VEH in the form of extracted electrical power across a suitable load (266 Ω). At low amplitude of external excitation (0.1g), the response of the system resembles that of a linear system and on increasing this excitation from 0.1g to 0.3g, the nonlinearity due to the effect of spring stretching comes into play, making the response of the system gradually non-resonant in nature. The response splits into two stable energy branches (on sweeping the frequency up and down, the response follows the high and low energy branch respectively) and the system can stay in either of the branches depending on the initial condition and the nature of frequency schedule. This multistable nature of the system enhances the operable bandwidth of the VEH.

We have considered Si-MEMS springs to hold the microcoil layer, which exhibits in-plane vibrations when subjected to external excitation. The mechanical damping of such MEMS spring structure

varies with different constituent materials, as well as with different structural designs. For example, [Nguyen 2010] obtained the mechanical damping of 2.53×10^{-4} N-s/m from the response curve fitting of a silicon MEMS spring architecture. For our analysis, we have considered here two different values of mechanical damping coefficient, 0.01 and 0.001, as typical values [Toshiyoshi 2019], keeping the external excitation amplitude fixed at 1g, to study the effect of this damping on the overall performance of the linear (as shown in Fig. 4(a)) and the nonlinear (spring-c) device. The half-power bandwidth of the nonlinear structure (25Hz) is approximately six times larger than that of the linear ones (4Hz) with 1g excitation. When the mechanical damping is high (0.01), both the linear and the nonlinear devices assembled in the topology-4 offers a power density of $0.61 \mu\text{W}/\text{cm}^3$ and $0.24 \mu\text{W}/\text{cm}^3$ with the linear and the nonlinear spring structures, respectively. However, the reduced mechanical damping factor of 0.001 aids in producing a power density of up to $52 \mu\text{W}/\text{cm}^3$ with the linear device (with 1g excitation amplitude) when it is assembled as topology-4. The low damping also aids in enhancing the power output from the nonlinear device, the spring-c maximizes the power density to $7.73 \mu\text{W}/\text{cm}^3$ with the compact topology-4.

So, it can be concluded that when the mechanical damping is relatively small, the EM coupling associated with the electrical damping dominates and influences the performance of the devices. The maximum power can be extracted from the harvester unit by reducing the mechanical damping to a point, comparable to the EM damping associated with the system [O'Donnell 2007]. A significant part of the mechanical damping consists of the frictional loss and the damping due to air drag. Vacuum packaging of the MEMS structures is a popular approach to circumvent the air damping [Elfrink 2010]. The mechanical damping could be also reduced by altering the spring architecture, e.g. by making comb like structures that reduces the air damping [Lu 2018]. Hence, to conclude, the most compact topology (topology-4) including the optimized patterns of micromagnets and coils can be used with the linear spring where the vibrations comprise of a single resonant peak, and those can be used with the optimized nonlinear spring (spring-c) for broadband vibrations.

IV. CONCLUSION

This letter presents the design of fully integrated MEMS EM-VEH with relatively high power density, which consists of an optimized patterned array of stripe shape magnets, and linear, nonlinear MEMS spring that carries the coil. Through analytical formulation and systematic finite element analysis, we have presented an approach to maximize the magnetic flux density in a precise location. Rectangular and square shaped micro-coils have been employed, the former demonstrating stronger EM interaction with the stripe micromagnets resulting in a dramatically improved EM coupling coefficient of $62.9 \text{mWb}/\text{m}$. A compact topology with designed linear spring produces a power density as high as $52 \mu\text{W}/\text{cm}^3$ at 1g acceleration with a low half power bandwidth. The nonlinear counterpart enhances the bandwidth almost six times to 25Hz at the cost of reduced power density. This detailed study opens up the scope for improving the performance of the overall device with further design optimization that will aid in powering the wireless sensor network.

ACKNOWLEDGMENT

The authors would like to thank Andreas Amann for the valuable discussions and Norah Dempsey, Frederico Orlandini-Keller for providing the data of sputtered magnetic material. This work is financially supported by a research grant from Science Foundation Ireland (SFI) and is co-funded under the European Regional Development Fund Grant Number 13/RC/2077. This is also part funded by the EU-H-2020 project 'Enables', Project ID: 730957 and TA 023.

REFERENCES

- Beeby S P and O'Donnell T (2009), "Electromagnetic Energy Harvesting " *Springer, Boston, MA*, Book Chapter pp. 129-161, doi: https://doi.org/10.1007/978-0-387-76464-1_5. Energy Harvesting Technologies.
- Coey J M D (2011), "Hard Magnetic Materials: A Perspective," *IEEE Transactions on Magnetics*, vol. 47, pp. 4671-4681, doi: 10.1109/TMAG.2011.2166975.
- Dempsey N M *et al.*, (2013), "High-coercivity Nd-Fe-B thick films without heavy rare earth additions", *Acta Materialia*, Vol. 61, pp. 4920-4927, ISSN 1359-6454, <https://doi.org/10.1016/j.actamat.2013.04.055>.
- Elfrink R *et al.*, (2010), "Vacuum-packaged piezoelectric vibration energy harvesters: damping contributions and autonomy for a wireless sensor system," *Journal of Micromechanics and Microengineering*, vol. 20, pp. 104001, doi: 10.1088/0960-1317/20/10/104001.
- Furlani E P (2001), "Chapter 4 - Permanent Magnet Applications," in *Permanent Magnet and Electromechanical Devices*, E. P. Furlani Ed. San Diego: Academic Press, pp. 207-333.
- Han M *et al.*, (2014), "Analysis of an in-plane electromagnetic energy harvester with integrated magnet array," *Sensors and Actuators A: Physical*, vol. 219, pp. 38-46, doi: <https://doi.org/10.1016/j.sna.2014.08.008>.
- Han M *et al.*, (2014), "Design and Fabrication of Integrated Magnetic MEMS Energy Harvester for Low Frequency Applications," *Journal of Microelectromechanical Systems*, vol. 23, pp. 204-212, doi: 10.1109/JMEMS.2013.2267773.
- Jamieson B *et al.*, (2013), "Device Geometry Effects in an Integrated Power Microinductor With a Ni₄Fe₅₅ Enhancement Layer," in *IEEE Transactions on Magnetics*, vol. 49, pp. 869-873, doi: 10.1109/TMAG.2012.2213826.
- Kuang Y *et al.*, (2017), "Energy harvesting during human walking to power a wireless sensor node," *Sensors and Actuators A: Physical*, vol. 254, pp. 69-77, doi: <https://doi.org/10.1016/j.sna.2016.11.035>.
- Kulkarni S *et al.*, (2006), "Vibration based electromagnetic micropower generator on silicon," *Journal of Applied Physics*, vol. 99, p. 08P511, doi: 10.1063/1.2176089.
- Keller F O, Dempsey N M (2021), Institut Néel (CNRS & Université Grenoble Alpes) *in preparation*.
- Lu Y *et al.*, (2018), "A power supply module for autonomous portable electronics: ultralow-frequency MEMS electrostatic kinetic energy harvester with a comb structure reducing air damping," *Microsystems & Nanoengineering*, vol. 4, p. 28, doi: 10.1038/s41378-018-0025-2.
- Lei Y and Wen Z (2015), "Study on effects of the damping ratio on output performance of micro electromagnetic vibration energy harvesters," *Microsystem Technologies*, vol. 21, pp. 221-226, doi: 10.1007/s00542-014-2114-y.
- Li Y *et al.*, (2020), "Electromagnetic vibrational energy harvester with microfabricated springs and flexible coils," *IEEE Transactions on Industrial Electronics*, pp. 1-1, doi: 10.1109/TIE.2020.2973911.
- Liao Q *et al.*, (2016), "Origin of thermal depolarization in piezoelectric ceramics," *Scripta Materialia*, vol. 115, pp. 14-18, doi: 10.1016/j.scriptamat.2015.12.030.
- Liu H *et al.*, (2014), "An In-Plane Approximated Nonlinear MEMS Electromagnetic Energy Harvester," in *Journal of Microelectromechanical Systems*, vol. 23, pp. 740-749, doi: 10.1109/JMEMS.2013.2281736.
- Mallick D *et al.*, (2014), "A nonlinear stretching based electromagnetic energy harvester on FR4 for wideband operation," *Smart Materials and Structures*, vol. 24, no. 1, p. 015013, doi: 10.1088/0964-1726/24/1/015013.
- Mallick D *et al.*, (2019), "Magnetic performances and switching behavior of Co-rich CoPtP micro-magnets for applications in magnetic MEMS," *Journal of Applied Physics*, vol. 125, p. 023902, doi: 10.1063/1.5063860.
- Miwatani N *et al.*, (2016), "Design Improvement For Preventing Discharge During Fabrication Of Electrostatic Energy Harvester," *Journal of Physics: Conference Series*, vol. 773, p. 012117, doi: 10.1088/1742-6596/773/1/012117.
- Nguyen D S *et al.*, (2010), "Fabrication and characterization of a wideband MEMS energy harvester utilizing nonlinear springs", *Journal of Micromechanics and Microengineering*, vol. 20, p. 125009, doi: 10.1088/0960-1317/20/12/125009.
- Nakano M *et al.*, (2015), "Nd-Fe-B Film magnets with thickness above 100 μm deposited on si substrates", *IEEE Trans. Magn.* Vol. 51, pp. 1-4, <https://doi.org/10.1109/TMAG.2015.2438099>.
- O'Donnell T *et al.*, (2007), "Scaling Effects for Electromagnetic Vibrational Power Generators," *CoRR*, vol. abs/0711.3316, doi: 10.1007/s00542-006-0363-0.
- Paul K *et al.*, (2021), "Tapered nonlinear vibration energy harvester for powering Internet of Things", *Applied Energy*, Volume 283, 116267, ISSN 0306-2619, <https://doi.org/10.1016/j.apenergy.2020.116267>.
- Roy S *et al.*, Mallick D, and Paul K (2019), "MEMS-Based Vibrational Energy Harvesting and Conversion Employing Micro-/Nano-Magnetics," *IEEE Transactions on Magnetics*, vol. 55, pp. 1-15, doi: 10.1109/TMAG.2019.2896105.
- Roy S *et al.*, "Broadband vibrational energy harvesting device combining multiple nonlinearity", U.S. Patent 10971986, April 6, 2021
- Toshiyoshi H *et al.*, (2019) MEMS vibrational energy harvesters, *Science and Technology of Advanced Materials*, vol. 20:1, pp. 124-143, DOI: 10.1080/14686996.2019.1569828
- Zablotskii V *et al.*, (2010), "High-Field Gradient Permanent Micromagnets for Targeted Drug Delivery with Magnetic Nanoparticles," *AIP Conference Proceedings*, vol. 1311, pp. 152-157, doi: 10.1063/1.3530005.